Available online at www.sciencedirect.com
SCIENCE DIRECT
Journal of Computational Physics 215 (2006) 41–58
JOURNAL OF COMPUTATIONAL PHYSICS
www.elsevier.com/locate/jcp

Spectral (finite) volume method for conservation laws on unstructured grids VI: Extension to viscous flow

Yuzhi Sun [a], Z.J. Wang [a,*], Yen Liu [b]

[a] Department of Aerospace Engineering, College of Engineering, Iowa State University, 2271 Howe Hall, Ames, IA 50011, United States
[b] NASA Ames Research Center, Moffett Field, CA 94035, United States

Received 17 July 2005; received in revised form 18 October 2005; accepted 20 October 2005
Available online 6 December 2005

Abstract

In this paper, the spectral volume (SV) method is extended to solve viscous flow governed by the Navier–Stokes equations. Several techniques to discretize the viscous fluxes have been tested, and a formulation similar to the local discontinuous Galerkin (DG) approach developed for the DG method has been selected in the present study. The SV method combines two key ideas, which are the bases of the finite volume and the finite element methods, i.e., the physics of wave propagation accounted for by the use of a Riemann solver and high-order accuracy achieved through high-order polynomial reconstructions within spectral volumes. The formulation of the SV method for a 2D advection-diffusion equation and the compressible Navier–Stokes equations is described. Accuracy studies are performed using problems with analytical solutions. The solver is used to compute laminar viscous flow problems to shown its potential.

MRI: 65M60; 65M70; 35L65

Keywords: High-order; Unstructured grid; Spectral finite volume; Navier–Stokes equations

1. Introduction

We continue the development of the spectral (finite) volume (SV) method for hyperbolic conservation laws on unstructured grids following the basic formulation [27], development for two-dimensional scalar conservation laws [28], one-dimensional systems and partition optimization [29], two-dimensional systems [30], and three-dimensional linear systems [14]. In the present study, the SV method is extended to compute viscous flows governed by the Navier–Stokes equations. The SV method belongs to a general class of Godunov-type finite volume method [11,26], which has been under development for several decades, and has become the state-of-the-art for the numerical solution of hyperbolic conservation laws. For a more detailed review of

DOI of original article: 10.1016/j.jcp.2003.09.012, 10.1016/j.jcp.2005.06.024.
* Corresponding author. Tel.: +1 515 294 1614; fax: +1 515 294 3262.
E-mail addresses: sunyuzhi@iastate.edu (Y. Sun), zjw@iastate.edu (Z.J. Wang), Yen.Liu@nasa.gov (Y. Liu).

0021-9991/$ - see front matter
doi:10.1016/j.jcp.2005.10.019

the literature on the Godunov-type method, refer to [27], and the references therein. Some widely used numerical methods for conservation laws such as the k-exact finite volume [2,10], the essentially non-oscillatory (ENO) [12,1], and weighted ENO [13] methods are also Godunov-type methods. The SV method is also related to a popular finite-element method for hyperbolic conservation laws, the discontinuous Galerkin (DG) method [5–8] in that multiple degrees of freedom are used in a single element. Comparisons between the DG and SV methods have been made recently [24,33]. The SV method avoids the volume integral required in the DG method. However, it does introduce more interfaces where more Riemann problems are solved. For 2D Euler equations, both methods seem to achieve similar efficiency [24]. Both the DG and SV methods are capable of achieving the optimal order of accuracy. The DG method usually has a lower error magnitude, but the SV method allows larger time steps. Due to its inherent property of subcell resolution, the SV method appears to capture discontinuities with a higher resolution than the DG method.

Ultimately, we wish to apply the SV method to perform large eddy simulation and direct numerical simulation of turbulent flow for problems with complex geometries. To achieve this goal, we must first find a technique to properly discretize the second-order viscous terms. In the second-order finite volume method, the solution gradients at an interface are usually computed by averaging the gradients of the neighboring cells sharing the face. For higher-order elements, special care has to be taken in computing the solution gradients. For example, Cockburn and Shu developed the so-called local discontinuous Galerkin method (LDG) to treat the second-order viscous terms and proved stability and convergence with error estimates [9] motivated by the successful numerical experiments of Bassi and Rebay [3]. Baumann and Oden [4], Oden et al. [16] introduced various penalty-type methods for the discretization of second-order viscous terms. Riviere et al. [17] analyzed three discontinuous Galerkin approximations for solving elliptic problems in two or three dimensions. More recently, Shu [22] summarized three different formulations for the diffusion equation, and Zhang and Shu [34] performed a Fourier type analysis for these three formulations. Recently, several formulations based on the successful LDG and penalty-type approaches have been developed and analyzed for the SV method using the 1D pure diffusion equation [25]. Three SV formulations, i.e., naïve formulation, local SV (LSV) and penalty SV (PSV) approaches, are tested. In the naïve formulation, the gradients on a face are obtained by averaging the gradients from the two cells sharing the face. It was found that the naïve formulation converges to the wrong solution, while the LSV and the PSV approaches are consistent, stable and convergent. It was shown that the LSV method achieved the optimal order of accuracy, i.e., $(k+1)$th order for degree k polynomial reconstructions. The PSV approach, however, achieved only kth order accuracy if k is even. Therefore, the LSV approach is selected for the extension to the Navier–Stokes equations in the present study. Before we attempt to solve the full 2D Navier–Stokes equations, the LSV formulation is further tested on 1D (both linear and non-linear) and 2D convection-diffusion equations.

The paper is therefore organized as follows. In Section 2, we describe the spectral volume formulation for the 2D convection-diffusion equation. The degeneration from 2D to 1D should be obvious. After that, the extension of the SV method to the Navier–Stokes equations is presented in Section 3. Section 4 presents numerical results including accuracy studies for the convection-diffusion equation. In addition, computations of laminar flows over a flat plate, a circular cylinder, and a NACA0012 airfoil are carried out, and results are compared with benchmark computations. Finally, conclusions and some possible future work are summarized in Section 5.

2. Spectral volume formulation for 2D convection-diffusion equation

For the sake of simplicity, the following 2D convection-diffusion equation is considered first in domain Ω with proper initial and boundary conditions

$$\frac{\partial u}{\partial t} + \nabla \cdot (\boldsymbol{\beta} u) - \nabla \cdot (\mu \nabla u) = 0, \tag{2.1}$$

where $\boldsymbol{\beta}$ is the convective velocity vector and μ is a positive diffusion coefficient. The computational domain Ω is discretized into N non-overlapping triangular cells. These cells, denoted as S_i, are called spectral volumes (SVs) in the SV method, i.e., $\Omega = \bigcup_{i=1}^{N} S_i$. An SV is further partitioned into a set of structured subcells, called control volumes (CVs), depending on the degree of the reconstruction polynomial. The partitions to be used in

this paper are shown in Fig. 1 for various degrees of reconstruction. The degrees-of-freedom (DOFs) in the SV method are the subcell-averages of the state variable. Let the jth CV of S_i be denoted by $C_{i,j}$. Following the local DG (LDG) approach [13,14,21], we define an auxiliary variable

$$q = \nabla u. \tag{2.2}$$

Eq. (2.1) then becomes

$$\frac{\partial u}{\partial t} + \nabla \cdot (\boldsymbol{\beta} u) - \nabla \cdot (\mu q) = 0. \tag{2.3}$$

Integrating (2.2) and (2.3) in $C_{i,j}$ and using the Gauss's (divergence) theorem, we obtain

$$\bar{q}_{i,j} V_{i,j} = \sum_{r=1}^{K} \int_{A_r} u \mathbf{n} \, \mathrm{d}A, \tag{2.4}$$

$$\frac{\mathrm{d}\bar{u}_{i,j}}{\mathrm{d}t} V_{i,j} + \sum_{r=1}^{K} \int_{A_r} \boldsymbol{\beta} u \cdot \mathbf{n} \, \mathrm{d}A - \sum_{r=1}^{K} \int_{A_r} \mu q \cdot \mathbf{n} \, \mathrm{d}A = 0, \tag{2.5}$$

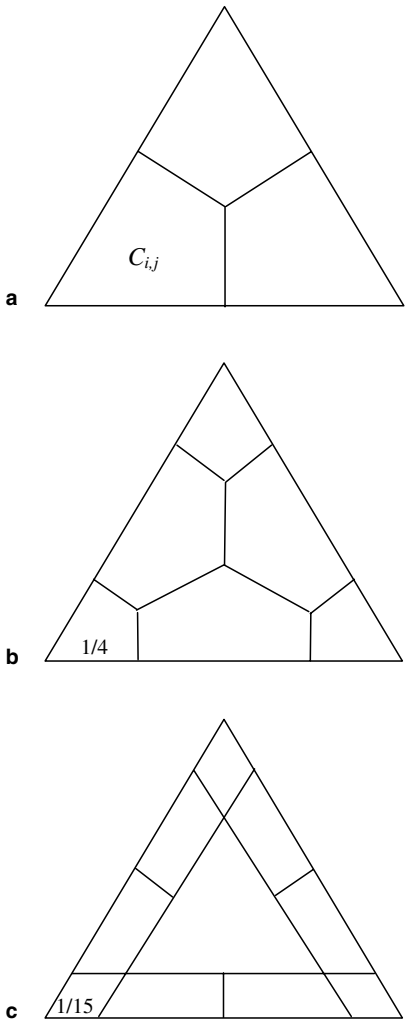

Fig. 1. Partitions of various orders in a triangular spectral volume. (a) Linear; (b) quadratic; and (c) cubic.

where $\bar{q}_{i,j}$ and $\bar{u}_{i,j}$ are the CV-averaged gradient and solution in $C_{i,j}$, K is the number of faces in $C_{i,j}$, and A_r represents the rth face of $C_{i,j}$ and $\mathbf{n}$ is the unit surface normal vector. Since the solution u is cell-wise continuous (i.e., continuous across the CVs inside a SV), u and q at SV boundaries are not well defined, and therefore they are replaced with the so-called "numerical fluxes" $\hat{u}$, $\tilde{u}$, and $\hat{q}$. Eqs. (2.4) and (2.5) thus become

$$\bar{q}_{i,j}V_{i,j} = \sum_{r=1}^{K} \int_{A_r} \hat{u}\mathbf{n}\,\mathrm{d}A, \tag{2.6}$$

$$\frac{\mathrm{d}\bar{u}_{i,j}}{\mathrm{d}t}V_{i,j} + \sum_{r=1}^{K} \int_{A_r} \boldsymbol{\beta}\tilde{u}\cdot\mathbf{n}\,\mathrm{d}A - \sum_{r=1}^{K} \int_{A_r} \mu\hat{q}\cdot\mathbf{n}\,\mathrm{d}A = 0. \tag{2.7}$$

For the inviscid flux, one can use an approximate Riemann solver such as the Rusanov [19] or Roe [18] Riemann solver. In the scalar case, both fluxes degenerate to the following upwind flux:

$$\tilde{u} = \begin{cases} u_{\mathrm{L}}, & \boldsymbol{\beta}\cdot\mathbf{n} > 0, \\ u_{\mathrm{R}}, & \boldsymbol{\beta}\cdot\mathbf{n} < 0, \end{cases} \tag{2.8}$$

where u_{L} and u_{R} are the solution at the left cell or the right cell of face A_r. The other two numerical fluxes are defined by alternating the direction in the following manner according to [9]:

$$\begin{aligned} \hat{u} &= u_{\mathrm{L}}, \\ \hat{q} &= q_{\mathrm{R}}, \end{aligned} \tag{2.9}$$

or

$$\begin{aligned} \hat{u} &= u_{\mathrm{R}}, \\ \hat{q} &= q_{\mathrm{L}}. \end{aligned} \tag{2.10}$$

In fact, both (2.9) and (2.10) are valid choices. For the sake of easy boundary treatment, (2.10) is selected in the present study since boundary faces are oriented in such a way that the normals all point out of the computational domain. In this case, we do not need a boundary condition for the gradients at all the boundary faces. Other aspects of the SV method are already described in the earlier papers [28,30], and details are not repeated here. For example, all the surface integrals in (2.6) and (2.7) are performed with appropriate Gauss quadrature formulas. For time integration, we use the third-order or fourth-order TVD (total variation diminishing) or SSP (strong-stability-preserving) Runge–Kutta schemes [20,23]. The time step is approximately modified in the 1D scalar case using

$$\Delta t = \frac{CFL}{\frac{|\beta|}{\Delta x} + \frac{\mu}{\Delta x^2}}, \tag{2.11}$$

where Δx is the cell size in 1D. In 2D, the time step is computed according to

$$\Delta t = \frac{CFL}{\sum_r \left(\frac{|\beta|A_r}{V} + \frac{\mu A_r^2}{V^2}\right)}. \tag{2.12}$$

3. Extension to the Navier–Stokes equations

With the description given for the convection-diffusion equation, the extension to the Navier–Stokes equations is straightforward. We consider the two-dimensional Navier–Stokes equations written in the conservative form

$$\frac{\partial Q}{\partial t} + \nabla\cdot\vec{F}_e(Q) - \nabla\cdot\vec{F}_v(Q,\nabla Q) = 0, \tag{3.1a}$$

where the conservative variables Q and the Cartesian components $f_e(Q)$ and $g_e(Q)$ of the inviscid flux vector $\vec{F}_e(Q)$ are given by

$$Q = \begin{Bmatrix} \rho \\ \rho u \\ \rho v \\ E \end{Bmatrix}, \quad f_e(Q) = \begin{Bmatrix} \rho u \\ \rho u^2 + p \\ \rho uv \\ u(E+p) \end{Bmatrix}, \quad g_e(Q) = \begin{Bmatrix} \rho v \\ \rho uv \\ \rho v^2 + p \\ v(E+p) \end{Bmatrix}. \tag{3.1b}$$

Here, ρ is the density, u and v are the velocity components in x and y directions, p is the pressure, and E is the total energy. The pressure is related to the total energy by

$$E = \frac{p}{\gamma - 1} + \frac{1}{2}\rho(u^2 + v^2) \tag{3.1c}$$

with a constant ratio of specific heats γ, which is taken to be 1.4 in all the simulations in this paper. The Cartesian components $f_v(Q, \nabla Q)$ and $g_v(Q, \nabla Q)$ of the viscous flux vector $\vec{F}_v(Q, \nabla Q)$ are given by

$$f_v(Q, \nabla Q) = \mu \cdot \begin{Bmatrix} 0 \\ 2u_x + \lambda(u_x + v_y) \\ v_x + u_y \\ u[2u_x + \lambda(u_x + v_y)] + v(v_x + u_y) + \frac{C_p}{P_r} T_x \end{Bmatrix}, \tag{3.1d}$$

$$g_v(Q, \nabla Q) = \mu \cdot \begin{Bmatrix} 0 \\ v_x + u_y \\ 2v_y + \lambda(u_x + v_y) \\ u(v_x + u_y) + v[2v_y + \lambda(u_x + v_y)] + \frac{C_p}{P_r} T_y \end{Bmatrix}, \tag{3.1e}$$

where μ is the dynamic viscosity, C_p is the specific heat at constant pressure, P_r is the Prandtl number, T is the temperature. Using the Stokes hypothesis, one obtains $\lambda = -2/3$. Again following the LDG approach, we define the following auxiliary variable:

$$G = \nabla Q. \tag{3.2}$$

Then Eq. (3.1a) becomes

$$\frac{\partial Q}{\partial t} + \nabla \cdot \vec{F}_e(Q) - \nabla \cdot \vec{F}_v(Q, G) = 0. \tag{3.3}$$

Integrating (3.2) and (3.3) in $C_{i,j}$ and using the Gauss's theorem, we obtain

$$\bar{G}_{i,j} V_{i,j} = \sum_{r=1}^{K} \int_{A_r} Q \mathbf{n} \, dA, \tag{3.4}$$

$$\frac{d\bar{Q}_{i,j}}{dt} V_{i,j} + \sum_{r=1}^{K} \int_{A_r} \vec{F}_e(Q) \cdot \mathbf{n} \, dA - \sum_{r=1}^{K} \int_{A_r} \vec{F}_v(Q, G) \cdot \mathbf{n} \, dA = 0. \tag{3.5}$$

Because Q and G are discontinuous at SV boundaries, the auxiliary flux Q in (3.4), inviscid and viscous fluxes in (3.5) are replaced by "numerical fluxes" $\hat{Q}$, $\hat{F}_e$ and $\hat{F}_v$. The auxiliary and viscous fluxes take the following form:

$$\hat{Q} \approx Q^R, \tag{3.6}$$

$$\hat{F}_v \approx \vec{F}_v\left((Q^L + Q^R)/2, G^L\right). \tag{3.7}$$

In (3.7), we also used Q^{L} instead of $(Q^{\mathrm{L}} + Q^{\mathrm{R}})/2$, with similar, but slightly less accurate results. The inviscid flux $\tilde{F}_e$ used here is the Roe flux splitting [18].

4. Numerical results

4.1. Accuracy study with 1D and 2D convection-diffusion equations

Extensive accuracy studies were carried out for both 1D and 2D convection and diffusion equations. In 1D, both linear and non-linear equations are employed, and problems with exact solutions are designed to test the local spectral volume (LSV) approach. These accuracy studies are presented next.

4.1.1. 1D linear convection-diffusion equation

The following linear equation is solved with SV schemes of various orders:

$$u_t + u_x - u_{xx} = 0,$$

subject to the initial condition of $u(x,0) = \sin(x)$ and periodic boundary condition. The computational domain is $[-\pi, \pi]$. The numerical simulation was carried out until $t = 1$. The L_1 and L_∞ errors are presented in Table 1. Note that the LSV approach is capable of achieving the optimum orders of accuracy in all cases.

4.1.2. 1D viscous Burger's equation

Consider

$$u_t + u \cdot u_x - \mu u_{xx} = 0, \quad x \in (0,1)$$

with the following initial and boundary conditions:

$$u(x,0) = -\tanh\left(\frac{x}{2\mu}\right),$$

$$u(0,t) = 0, \quad u(1,t) = -\tanh\left(\frac{1}{2\mu}\right).$$

The problem has the following exact solution:

$$u(x,t) = -\tanh\left(\frac{x}{2\mu}\right).$$

The simulation is conducted until $t = 1$ with various SV schemes. The L_1 and L_∞ errors are presented in Table 2. Note that the LSV approach is again capable of achieving the optimum orders of accuracy in all cases.

Table 1
L_1 and L_∞ errors and orders of accuracy for 1D linear convection and diffusion equation (at $t = 1.0$)

Order	Number of cells	L_1 error	L_1 order	L_∞ error	L_∞ order
2	10	7.60e − 03	–	9.97e − 03	–
	20	2.07e − 03	1.88	2.89e − 03	1.79
	40	5.46e − 04	1.92	7.86e − 04	1.88
	80	1.40e − 04	1.96	2.04e − 04	1.95
3	10	3.83e − 04	–	5.37e − 04	–
	20	4.55e − 05	3.07	6.64e − 05	3.02
	40	5.57e − 06	3.03	8.16e − 06	3.02
	80	6.89e − 07	3.02	1.01e − 06	3.01
4	10	1.24e − 05	–	1.85e − 05	–
	20	7.92e − 07	3.97	1.17e − 06	3.98
	40	5.01e − 08	3.98	7.43e − 08	3.98
	80	3.15e − 09	3.99	4.69e − 09	3.99

Table 2
L_1 and L_∞ errors and orders of accuracy for 1D viscous Burger's equation (at $t = 1.0$)

Order	Number of cells	L_1 error	L_1 order	L_∞ error	L_∞ order
2	10	2.12e − 03	–	1.22e − 02	–
	20	6.16e − 04	1.78	4.30e − 03	1.50
	40	1.73e − 04	1.83	1.33e − 03	1.69
	80	4.76e − 05	1.86	3.66e − 04	1.86
3	10	4.84e − 04	–	3.43e − 03	–
	20	7.62e − 05	2.67	5.25e − 04	2.71
	40	1.04e − 05	2.87	7.06e − 05	2.89
	80	1.36e − 06	2.93	9.12e − 06	2.95
4	10	3.17e − 05	–	2.16e − 04	–
	20	1.49e − 06	4.41	9.53e − 06	4.50
	40	7.31e − 08	4.35	8.62e − 07	3.47
	80	4.22e − 09	4.11	6.20e − 08	3.80

4.1.3. 1D fully nonlinear equation

Further, we consider the following fully nonlinear equation:

$$u_t + u \cdot u_x - \frac{1}{2}(u \cdot u_x)_x = 0 \quad x \in (0,1)$$

with the following initial and boundary conditions:

$$u(x,0) = e^x;$$
$$u(0,t) = 1, \quad u(1,t) = e.$$

The problem has the following exact solution $u(x,t) = e^x$.

The simulation was carried out until $t = 1.0$ with various SV schemes. The L_1 and L_∞ errors are presented in Table 3. Note that the LSV approach is again capable of achieving the optimum order of accuracy in all cases.

4.1.4. 2D linear convection and diffusion equation

We also tested the LSV method on a 2D linear convection-diffusion equation written as

$$u_t + c(u_x + u_y) - \mu(u_{xx} + u_{yy}) = 0, \quad (x,y) \in (-1,1) \times (-1,1); \;\; c = 1, \;\; \mu = 0.01$$

with the initial condition $u(x,y,0) = \sin(\pi(x+y))$ and periodic boundary condition. The exact solution is $u(x,y,t) = \mathrm{e}^{-2\pi\mu t}\sin(\pi(x+y-2ct))$. Two meshes, one regular and irregular as shown in Fig. 2, were used

Table 3
L_1 and L_∞ errors and orders of accuracy for the fully nonlinear equation (at $t = 1.0$)

Order	Number of cells	L_1 error	L_1 order	L_∞ error	L_∞ order
2	10	9.52e − 04	–	2.1e − 03	–
	20	2.53e − 04	1.91	6.12e − 04	1.78
	40	6.52e − 05	1.96	1.65e − 04	1.89
	80	1.65e − 05	1.98	4.27e − 05	1.95
3	10	9.32e − 06	–	2.92e − 05	–
	20	1.22e − 06	2.93	3.99e − 06	2.87
	40	1.56e − 07	2.97	5.21e − 07	2.94
	80	1.97e − 08	2.99	6.65e − 08	2.97
4	10	6.30e − 08	–	2.37e − 07	–
	20	4.07e − 09	3.95	1.64e − 08	3.85
	40	2.59e − 10	3.97	1.07e − 09	3.94
	80	1.63e − 11	3.99	6.81e − 11	3.97

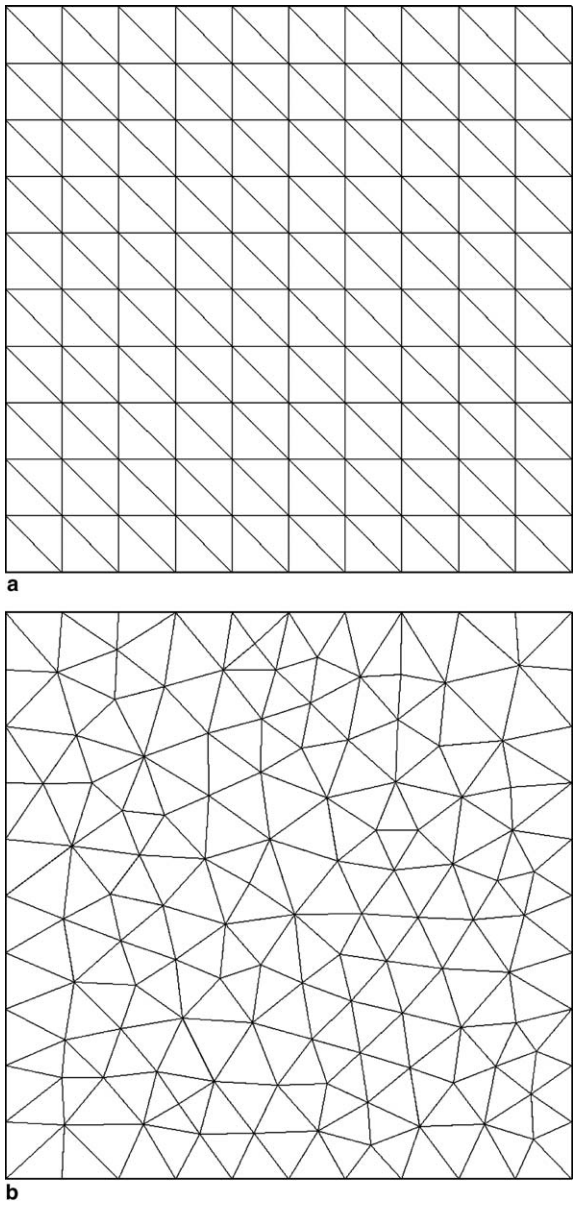

Fig. 2. (a) Regular and (b) irregular "$10 \times 10 \times 2$" computational grids.

in this test. The recorded L_1 and L_∞ errors in Table 4 for the regular mesh show that the LSV approach is capable of achieving the optimum orders of accuracy in all cases. The L_1 and L_∞ errors for the irregular mesh are presented in Table 5, again with nearly optimum convergence for all the schemes.

4.2. Laminar flow over a flat plate

We consider the laminar flow on an adiabatic flat plate characterized by a free stream Mach number $M = 0.3$ and by a Reynolds number based on the free stream condition and on the plate length $Re = 10{,}000$. The length of the plate is set to be $L = 1.0$. At $x = 1.0$, the thickness of the boundary layer δ is estimated to be

Table 4
L_1 and L_∞ errors and orders of accuracy for the 2D convection-diffusion equation (at $t = 1.0$ on regular mesh)

Order	Grid	L_1 error	L_1 order	L_∞ error	L_∞ order
2	$10 \times 10 \times 2$	3.73e − 02	–	5.35e − 02	–
	$20 \times 20 \times 2$	8.60e − 03	2.12	1.28e − 02	2.06
	$40 \times 40 \times 2$	2.16e − 03	1.99	3.25e − 03	1.98
	$80 \times 80 \times 2$	5.36e − 04	2.01	8.11e − 04	2.00
3	$10 \times 10 \times 2$	2.79e − 03	–	3.91e − 03	–
	$20 \times 20 \times 2$	3.40e − 04	3.04	5.10e − 04	2.94
	$40 \times 40 \times 2$	4.16e − 05	3.03	6.31e − 05	3.01
	$80 \times 80 \times 2$	5.21e − 06	3.00	7.97e − 06	2.98
4	$10 \times 10 \times 2$	4.14e − 05	–	5.72e − 05	–
	$20 \times 20 \times 2$	2.47e − 06	4.07	3.37e − 06	4.09
	$40 \times 40 \times 2$	1.47e − 07	4.07	1.95e − 07	4.11
	$80 \times 80 \times 2$	8.45e − 09	4.12	1.14e − 08	4.10

$$\delta|_{x=1.0} = 5 \cdot \sqrt{\frac{\mu \cdot x}{\rho_\infty \cdot u_\infty}}\Bigg|_{x=1.0} = 0.05.$$

Therefore, the size of computational domain in the y-direction is chosen to be 20 times the boundary layer thickness at $x = 1.0$ such that the flow at the top boundary is nearly inviscid. The range of computational domain in the x-direction is $[-1, 1]$. At the inlet, the free stream condition is imposed. At the top and exit boundaries, the static pressure is fixed. Since there is a singularity around the leading edge of the flat plate, the mesh is clustered in both the x and y directions to reduce its effects on the computational results. The computations were performed on three triangular meshes, coarse mesh (208 cells) with eight cells along the plate, medium mesh (832 cells) with 16 cells along the plate, and fine mesh (3328 cells) with 32 cells along the plate.

In the y direction of the coarse mesh, two cells are generated within the boundary layer near the end of the plate to test the resolution of the boundary layer. The grid sizes in the x and y directions around the leading edge of the plate are almost the same. Fig. 3 shows the three different meshes used in the numerical simulations. Figs. 4–6 show the velocity profiles at the end of the plate, with comparison to the Blasius solution, computed with 2nd, 3rd and 4th order SV schemes. The non-dimensional wall distance is defined as $y^* = y \cdot \sqrt{\frac{\rho_\infty \cdot U_\infty}{\mu \cdot x}}$. Furthermore, the computed skin friction profiles are also compared with the Blasius solution in Figs. 7–9. Note that the agreement gets better with grid refinements, and with higher order reconstructions.

4.3. Subsonic viscous flow over a circular cylinder

When a fluid flows over an isolated cylindrical solid barrier and the Reynolds number is great than about 50, vortices are shed on the down-stream side. The vortices trail behind the cylinder in two rolls, alternatively

Table 5
L_1 and L_∞ errors and orders of accuracy for the 2D convection-diffusion equation ($t = 1.0$ on irregular mesh)

Order	Grid	L_1 error	L_1 order	L_∞ error	L_∞ order
2	$10 \times 10 \times 2$	5.45e − 02	–	9.26e − 02	–
	$20 \times 20 \times 2$	1.43e − 02	1.93	2.44e − 02	1.92
	$40 \times 40 \times 2$	3.47e − 03	2.04	6.03e − 03	2.02
	$80 \times 80 \times 2$	8.07e − 04	2.10	1.42e − 03	2.09
3	$10 \times 10 \times 2$	5.43e − 03	–	9.94e − 03	–
	$20 \times 20 \times 2$	6.75e − 04	3.01	1.36e − 03	2.87
	$40 \times 40 \times 2$	8.45e − 05	3.00	1.76e − 04	2.95
	$80 \times 80 \times 2$	1.12e − 05	2.92	2.40e − 05	2.87
4	$10 \times 10 \times 2$	1.24e − 04	–	3.87e − 04	–
	$20 \times 20 \times 2$	5.77e − 06	4.43	2.51e − 05	3.95
	$40 \times 40 \times 2$	2.27e − 07	4.67	1.44e − 06	4.12
	$80 \times 80 \times 2$	1.67e − 08	3.76	7.83e − 08	4.20

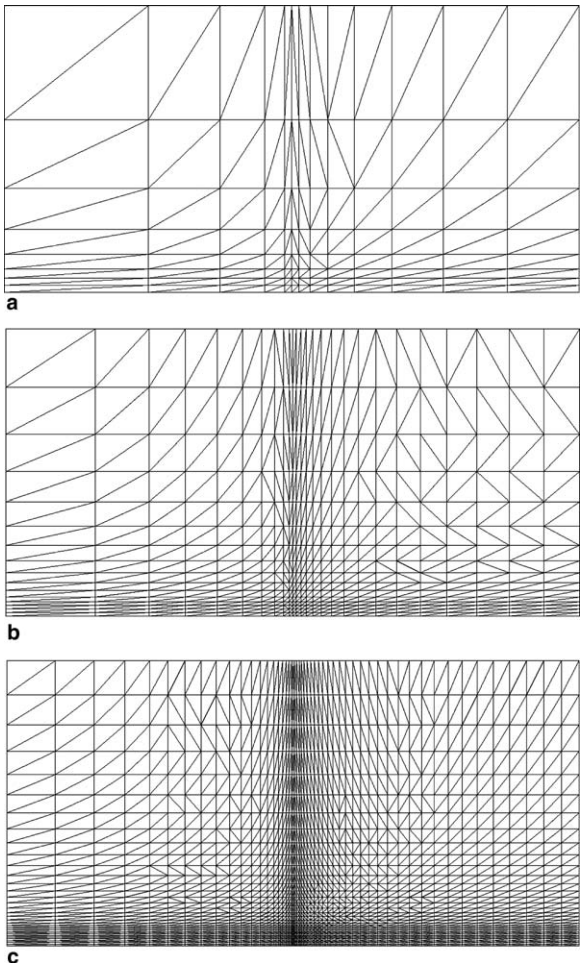

Fig. 3. Meshes for the flat plate boundary layer case: (a) coarse mesh, (b) medium mesh, and (c) fine mesh.

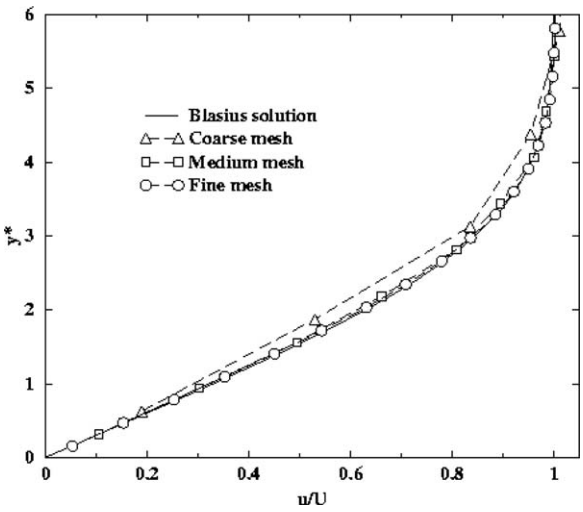

Fig. 4. *U*-velocity profiles for the flat plate case with linear SV.

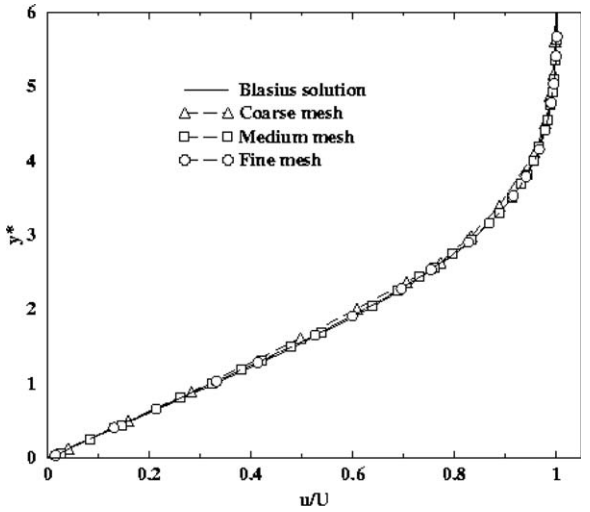

Fig. 5. *U*-velocity profiles for the flat plate case with quadratic SV.

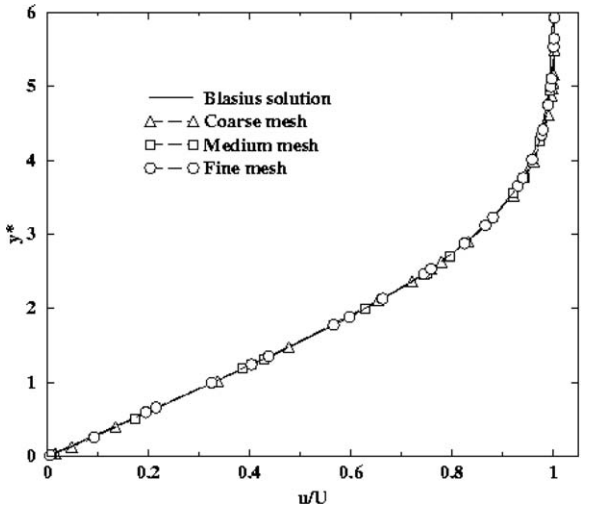

Fig. 6. Velocity profiles for the flat plate case with cubic SV.

from the top or the bottom of the cylinder. This vortex trail is called the Von Karman vortex street or Karman street after Von Karman's 1912 mathematical description of the phenomenon. Since then, many numerical and experimental studies have focused on the dynamics of vortex street formation in the near wake. Measured values of the Strouhal number of the vortex shedding frequency at various Reynolds numbers can be found in [32], where the Strouhal number is defined as $S = \frac{f_v \cdot D_c}{V}$. Here, D_c is the diameter of the cylinder, f_v the frequency of vortex shedding, and V the free stream velocity. Let the center of the cylinder be located at the origin, and the diameter be 1. The computational domain is selected to be $(-10, 16) \times (-10, 10)$, and the computational grid is displayed in Fig. 10. The grid has a total of 3516 cells.

The flow is assumed subsonic with a free stream Mach number $M = 0.2$, and the Reynolds number based on the free stream condition and the cylinder diameter is $Re = 75$. The cylinder is assumed to be adiabatic. In order to trigger the nonsymmetric vortex shedding, the initial condition has a small upward velocity component. Both the 3rd and 4th order SV schemes were employed in the simulations, and the results are nearly identical. After a sufficiently long time, the effects of the initial condition propagate out of the computational domain, and a periodic shedding of vortices is observed. Instantaneous contours of entropy, and vorticity

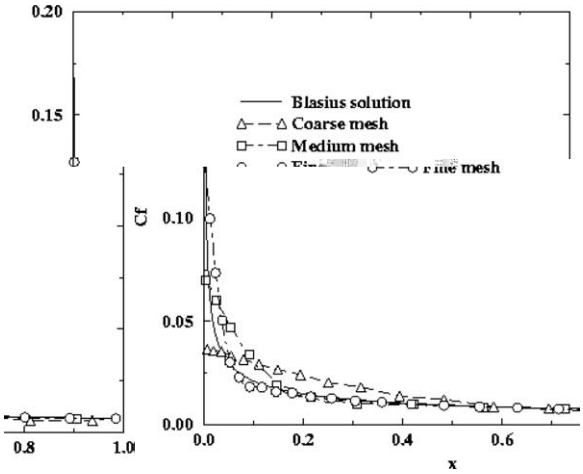

Fig. 7. Skin friction coefficients along a flat plate with linear SV.

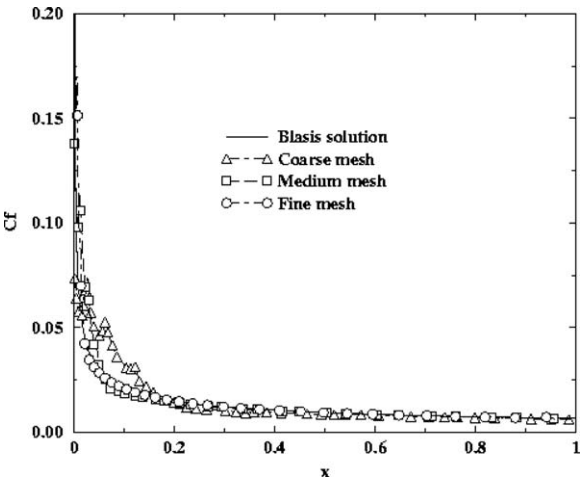

Fig. 8. Skin friction coefficients along a flat plate with quadratic SV.

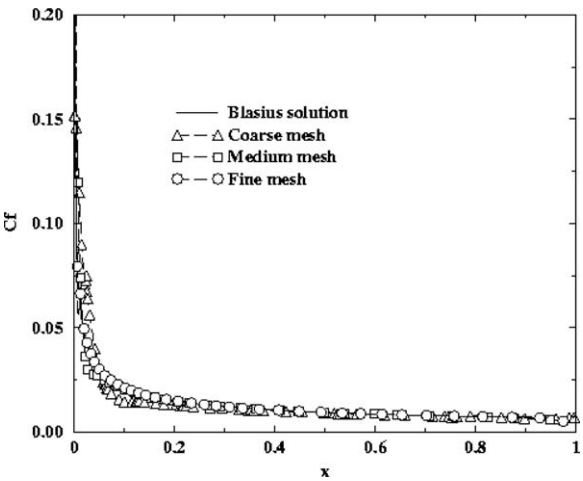

Fig. 9. Skin friction coefficients along a flat plate with cubic SV.

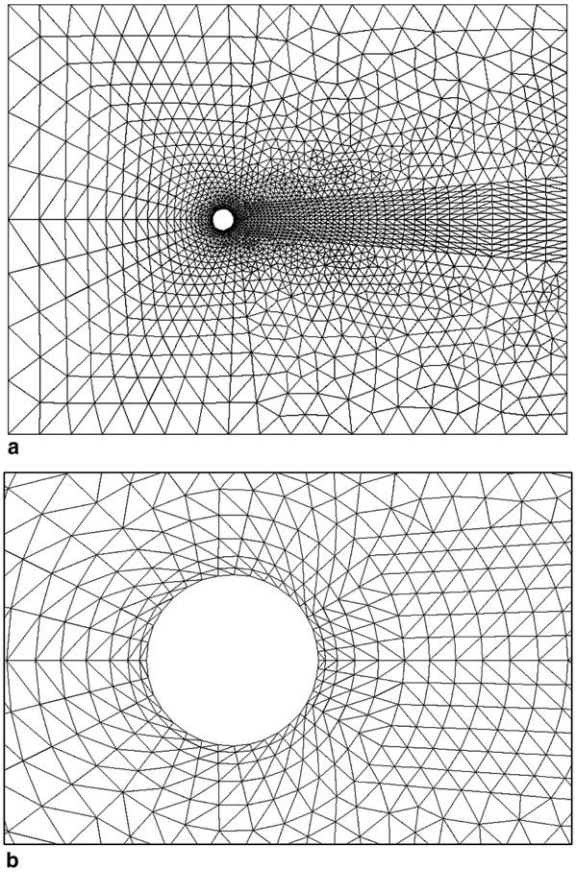

Fig. 10. Grid for the case of subsonic flow over a circular cylinder: (a) global grid and (b) grid near the cylinder.

showing the Von Karman vortex street generated by the cylinder are presented in Figs. 11 and 12. The periodic nature of the flow is shown in Fig. 13, which plots the pressure as a function of time calculated at (*10, 1*). The period (and thus the frequency) of the oscillations can be found from the pressure history. Based on the computed frequency, the Strouhal number is found to be *0.151*, which agrees well with the measured value of 0.148, found in [32].

4.4. Laminar flow around a NACA0012 airfoil

In this test, we consider a subsonic viscous flow problem over the NACA0012 airfoil at an angle of attack $\alpha = 0°$, free stream Mach number $M = 0.5$, and Reynolds number $Re = 5000$. This is a widely used validation

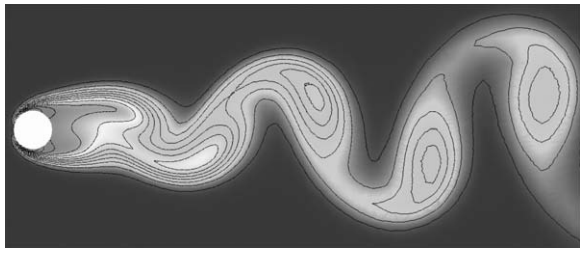

Fig. 11. Instantaneous entropy contours for $M = 0.2$ flow over a circular cylinder at $Re = 75$.

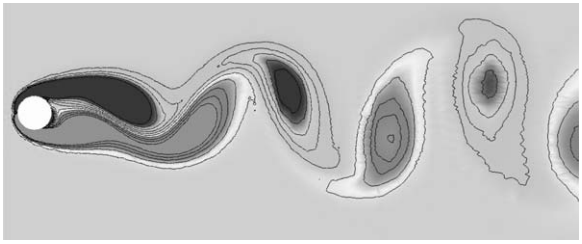

Fig. 12. Instantaneous vorticity contours for $M = 0.2$ flow over a circular cylinder at $Re = 75$.

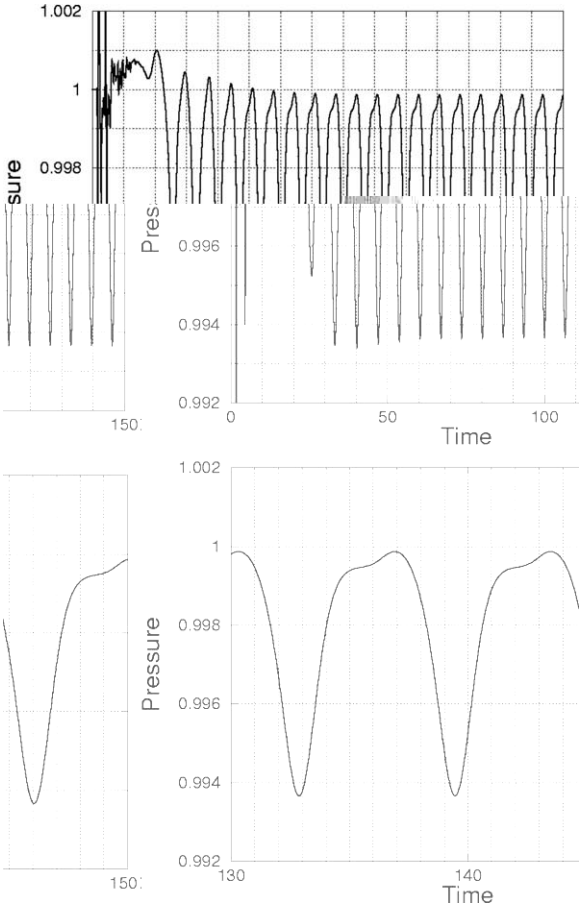

Fig. 13. Pressure history at $(x, y) = (10, 1)$ for $M = 0.2$ flow over a circular cylinder at $Re = 75$.

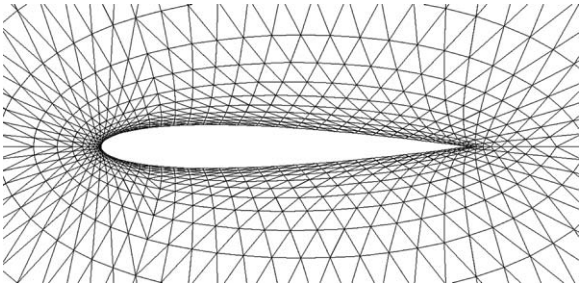

Fig. 14. Computational grid for subsonic viscous flow over the NACA0012 airfoil.

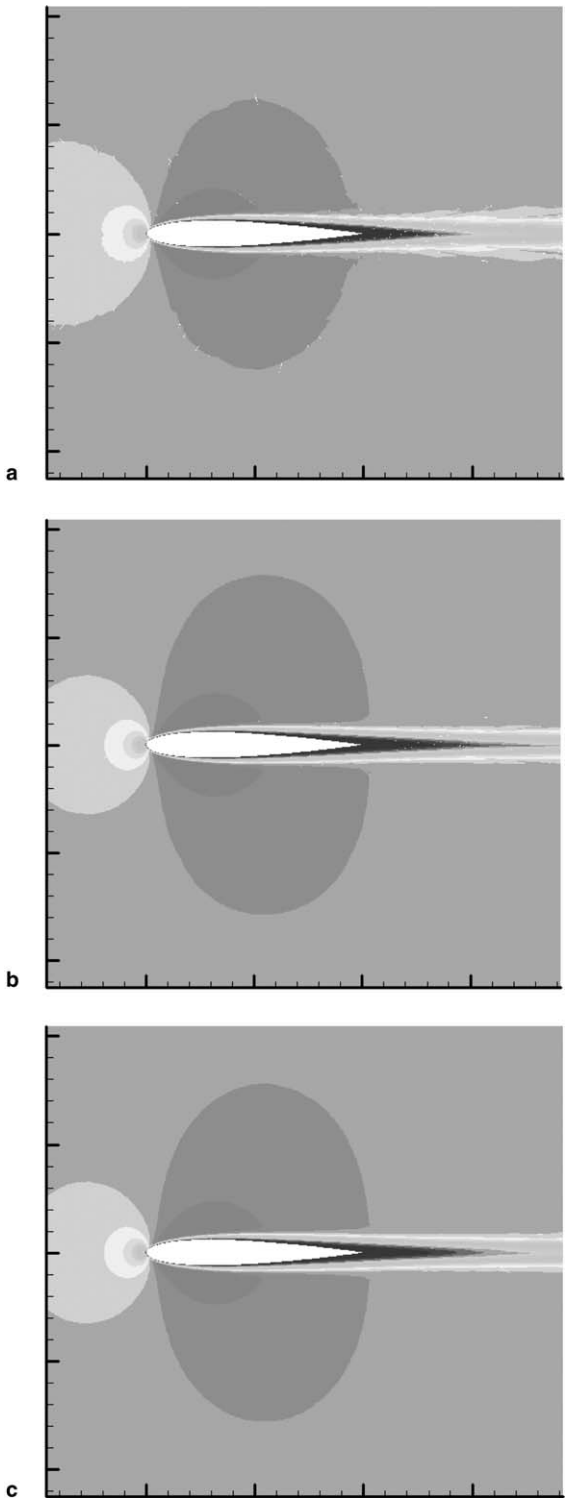

Fig. 15. Mach contours around the NACA0012 airfoil with various SV schemes ($Re = 5000$, $M = 0.5$, $\alpha = 0°$). (a) 2nd order; (b) 3rd order; and (c) 4th order.

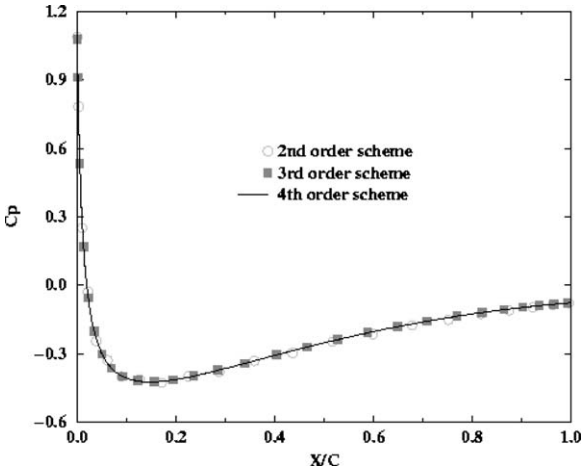

Fig. 16. Pressure coefficient distributions along the NACA0012 airfoil ($Re = 5000$, $M = 0.5$, $\alpha = 0°$).

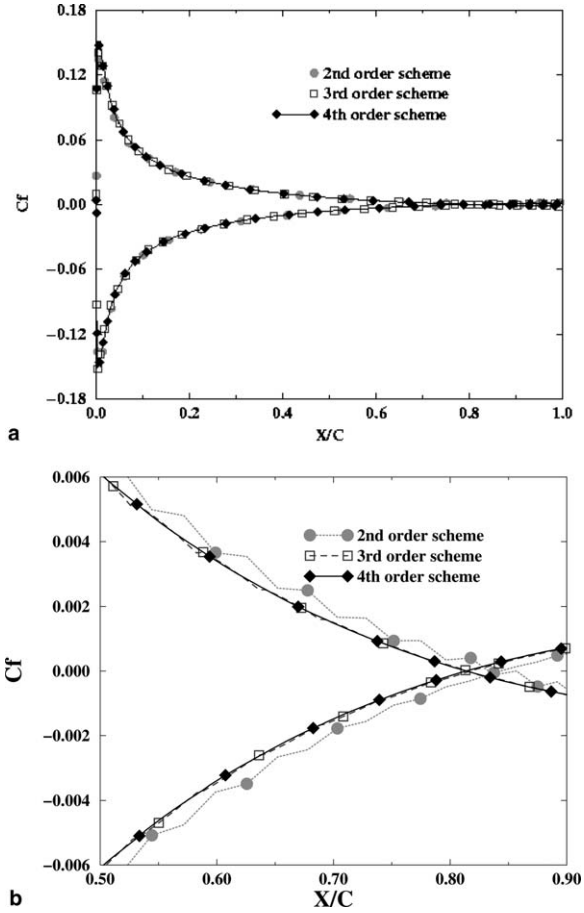

Fig. 17. Skin friction coefficient distributions along the NACA0012 airfoil ($Re = 5000$, $M = 0.5$, $\alpha = 0°$).

case for viscous flow solvers [15]. The computational grid is displayed in Fig. 14, which is generated from the triangulation of a 64×16 O-grid. The larger number refers to the number of cells distributed along the airfoil surface and the smaller one the number of cells in the radial direction. The grid extents about 20 chords away form the airfoil. The computations were performed using linear, quadratic and cubic SVs. The wall is assumed

to be non-slip and adiabatic, and is represented by a cubic curve [31]. The Reynolds number is near the upper limit for a steady laminar flow. A distinguishing feature of this test case is the separation region of the flow occurring near the trailing edge, which causes the formation of a small recirculation bubble that extends in the near-wake region of the airfoil.

Fig. 15 shows the Mach contours computed with linear, quadratic and cubic SVs. It is obvious that the solution is getting smoother and smoother with the increasing of the order of polynomial reconstruction, indicating the solution is more accurate. Figs. 16 and 17 show the pressure coefficient (C_p) and skin friction coefficient (C_f) distributions along the airfoil computed with linear, quadratic, and cubic SVs. Note that the agreement in the computed C_p profiles is excellent with the 2nd, 3rd and 4th order schemes. There is also close agreement in the computed C_f profiles, indicating the numerical results are approaching order-independence. It is obvious from Fig. 17(b) that the 3rd and 4th order SV schemes predicted nearly the same separation point.

5. Conclusions

The SV method is successfully extended to the Navier–Stokes equations by following a mixed formulation named the local discontinuous Galerkin approach originally developed for the DG method. The approach, which is named the local SV (LSV) approach, is tested extensively for 1D and 2D convection-diffusion equations using a serious of accuracy studies. All tests indicated that the formulation is capable of achieving the formal optimum order of accuracy in both the L_1 and L_∞ norms. The LSV approach is then implemented and tested for the Navier–Stokes equations, and used to compute several benchmark viscous flow problems. Good agreement has been achieved with analytical solutions or other simulations. Work is now underway to extend the SV method to three-dimensional Navier–Stokes equations, and to develop more efficient implicit solution algorithms to speed up the convergence rate to the steady state.

Acknowledgements

The first two authors gratefully acknowledge a start-up fund provided by the Department of Aerospace Engineering, College of Engineering of Iowa State University. The work is also partially funded by the Department of Energy under contract DE-FG02-05ER25677.

References

[1] R. Abgrall, On essentially non-oscillatory schemes on unstructured meshes: analysis and implementation, J. Comput. Phys. 114 (1994) 45–58.
[2] T.J. Barth, P.O. Frederickson, High-order solution of the Euler equations on unstructured grids using quadratic reconstruction, AIAA Paper No. 90-0013, 1990.
[3] F. Bassi, S. Rebay, A high-order accurate discontinuous finite element method for the numerical solution of the compressible Navier–Stokes equations, J. Comput. Phys. 131 (1997) 267–279.
[4] C.E. Baumann, J.T. Oden, A discontinuous *hp* finite element method for convection-diffusion problems, Comput. Meth. Appl. Mech. Eng. 175 (1999) 311–341.
[5] B. Cockburn, C.-W. Shu, TVB Runge–Kutta local projection discontinuous Galerkin finite element method for conservation laws II: general framework, Math. Comput. 52 (1989) 411–435.
[6] B. Cockburn, S.-Y. Lin, C.-W. Shu, TVB Runge–Kutta local projection discontinuous Galerkin finite element method for conservation laws III: one-dimensional systems, J. Comput. Phys. 84 (1989) 90–113.
[7] B. Cockburn, S. Hou, C.-W. Shu, TVB Runge–Kutta local projection discontinuous Galerkin finite element method for conservation laws IV: the multidimensional case, Math. Comput. 54 (1990) 545–581.
[8] B. Cockburn, C.-W. Shu, The Runge–Kutta discontinuous Garlerkin method for conservation laws V: multidimensional systems, J. Comput. Phys. 141 (1998) 199–224.
[9] B. Cockburn, C.-W. Shu, The local discontinuous Galerkin method for time-dependent convection diffusion system, SIAM J. Numer. Anal. 35 (1998) 2440–2463.
[10] M. Delanaye, Yen Liu, Quadratic reconstruction finite volume schemes on 3D arbitrary unstructured polyhedral grids, AIAA Paper No. 99-3259-CP, 1999.
[11] S.K. Godunov, A finite-difference method for the numerical computation of discontinuous solutions of the equations of fluid dynamics, Mat. Sb. 47 (1959) 271.

[12] A. Harten, B. Engquist, S. Osher, S. Chakravarthy, Uniformly high order essentially non-oscillatory schemes III, J. Comput. Phys. 71 (1987) 231.
[13] C. Hu, C.-W. Shu, Weighted essentially non-oscillatory schemes on triangular meshes, J. Comput. Phys. 150 (1999) 97–127.
[14] Y. Liu, M. Vinokur, Z.J. Wang, Spectral (finite) volume method for conservation laws on unstructured grids V: extension to three-dimensional systems, J. Comput. Phys., in press.
[15] Numerical simulation of compressible Navier–Stokes equations-external 2D flows around a NACA0012 airfoil, in GAMM Workshop, December 4–6, 1985, Nice, France (Edt. INRIA, Centre de Rocquefort, de Renes et de Sophia-Antipolis, 1986).
[16] J.T. Oden, I. Babuska, C.E. Baumann, A discontinuous *hp* finite element method for diffusion problems, J. Comput. Phys. 146 (1998) 491–519.
[17] B. Riviere, M. Wheeler, V. Girault, A priori error estimates for finite element methods based on discontinuous approximation spaces for elliptic problems, SIAM J. Numer. Anal. 39 (2001) 902–931.
[18] P.L. Roe, Approximate Riemann solvers, parameter vectors, and difference schemes, J. Comput. Phys. 43 (1981) 357–372.
[19] V.V. Rusanov, Calculation of interaction of non-steady shock waves with obstacles, J. Comput. Math. Phys. USSR 1 (1961) 267–279.
[20] C.-W. Shu, Total-variation-diminishing time discretizations, SIAM J. Sci. Stat. Comput. 9 (1988) 1073–1084.
[21] C.-W. Shu, Essentially non-oscillatory and weighted essentially non-oscillatory schemes for hyperbolic conservation laws, in: B. Cockburn, C. Johnson, C.-W. Shu, E. Tadmor (Eds.), Advanced Numerical Approximation of Nonlinear Hyperbolic Equations, in: A. Quarteroni (Ed.), Lecture Notes in Mathematics, vol. 1697, Springer, Berlin, 1998, pp. 325–432.
[22] C.-W. Shu, Different formulations of the discontinuous Galerkin method for the viscous terms, in: Z.-C. Shi, M. Mu, W. Xue, J. Zou (Eds.), Advances in Scientific Computing, Science Press, 2001, pp. 144–145.
[23] R.J. Spiteri, S.J. Ruuth, A new class of optimal high-order strong-stability-preserving time discretization methods, SIAM J. Numer. Anal. 40 (2002) 469–491.
[24] Y. Sun, Z.J. Wang, Evaluation of discontinuous Galerkin and spectral volume methods for scalar and system conservation laws on unstructured grid, Int. J. Numer. Meth. Fluids 45 (8) (2004) 819–838.
[25] Y. Sun, Z.J. Wang, Formulations and analysis of spectral volume method for the diffusion equation, Commun. Numer. Meth. Eng. 20 (12) (2004) 927–937.
[26] B. van Leer, Towards the ultimate conservative difference scheme V. a second-order sequel to Godunov's method, J. Comput. Phys. 32 (1979) 101–136.
[27] Z.J. Wang, Spectral (finite) volume method for conservation laws on unstructured grids: basic formulation, J. Comput. Phys. 178 (2002) 210.
[28] Z.J. Wang, Yen Liu, Spectral (finite) volume method for conservation laws on unstructured grids II: extension to two-dimensional scalar equation, J. Comput. Phys. 179 (2002) 665–697.
[29] Z.J. Wang, Yen Liu, Spectral (finite) volume method for conservation laws on unstructured grids III: one-dimensional systems and partition optimization, J. Sci. Comput. 20 (2004) 137–157.
[30] Z.J. Wang, Y. Liu, L. Zhang, Spectral (finite) volume method for conservation laws on unstructured grids IV: extension to two-dimensional systems, J. Comput. Phys. 194 (2004) 716–741.
[31] Z.J. Wang, Y. Liu, Extension of the spectral volume method to high-order boundary representation, J. Comput. Phys. 211 (2006) 154–178.
[32] C.H.K. Williamson, Oblique and parallel modes of vortex shedding in the wake of a cylinder at low Reynolds number, J. Fluid Mech. 206 (1989) 579.
[33] M. Zhang, C.-W. Shu, An analysis of and a comparison between the discontinuous Galerkin and spectral finite volume method, Comput. Fluid 34 (2005) 581–592.
[34] M. Zhang, C.-W. Shu, An analysis of three different formulations of the discontinuous Galerkin method for diffusion equations, Math. Models Meth. Appl. Sci. 13 (2003) 395–413.